Amoako-Yirenkyi et al. *Advances in Difference Equations* (2016) 2016:238
DOI 10.1186/s13662-016-0946-8

Advances in Difference Equations
a SpringerOpen Journal

RESEARCH Open Access

A new construction of a fractional derivative mask for image edge analysis based on Riemann-Liouville fractional derivative

Peter Amoako-Yirenkyi[1,2*], Justice Kwame Appati[1] and Isaac Kwame Dontwi[1,2]

*Correspondence:
amoakoyirenkyi@knust.edu.gh
[1]Department of Mathematics, Kwame Nkrumah University of Science and Technology, Kumasi, Ghana
[2]Scientific and Technical Computing Centre, National Institute for Mathematical Sciences, Kumasi, Ghana

Abstract

We present a new way of constructing a fractional-based convolution mask with an application to image edge analysis. The mask was constructed based on the Riemann-Liouville fractional derivative which is a special form of the Srivastava-Owa operator. This operator is generally known to be robust in solving a range of differential equations due to its inherent property of memory effect. However, its application in constructing a convolution mask can be devastating if not carefully constructed. In this paper, we show another effective way of constructing a fractional-based convolution mask that is able to find edges in detail quite significantly. The resulting mask can trap both local discontinuities in intensity and its derivatives as well as locating Dirac edges. The experiments conducted on the mask were done using some selected well known synthetic and Medical images with realistic geometry. Using visual perception and performing both mean square error and peak signal-to-noise ratios analysis, the method demonstrated significant advantages over other known methods.

Keywords: convolution; fractional integral; fractional derivative; edge detection; Riemann-Liouville

1 Introduction

Image edge analysis constitutes a set of mathematical methods which aim at identifying points in a digital image at which the image brightness changes sharply (point of discontinuities). The organization of these points into a set of curved line segments then becomes the edge. With no doubt, detecting these points and subsequently constructing an edge map is one of the most common and fundamental operations in image processing and analysis since it is consistent with the human perception and serves as the first step in image understanding and interpretation. They provide useful structural [1, 2] information, which can be used for feature extraction, object identification and region segmentation. This information, by common practice, is extracted by developing a convolution mask mostly known as the gradient operator which is a relatively smaller two dimensional array where each pixel value of the original image is modified according to the value of the neighborhood around the pixel of interest (POI) [3]. However, there are other forms, such

as the segmentation- and transform-based operators, which could also be used for edge extraction. The definitions of particular operators in any of these three categories have their own pros and cons. Although several studies [4–7] have been done to improve these methods for edge detection, they still produce edges with some compromise in accuracy, completeness, complexity, connectedness, and smoothness. A recent study [8] by Guo and Lai confirmed how gradient operators resist just low-level noise but tend to mistakenly detect fake edges in the presence of excessive noise or artifacts. In an attempt to resolve some of these issues other operators [9–12] mostly based on fractional calculus with improved characteristics over the classical methods like Canny and Prewitt have been proposed.

In particular the fractional-based operators have been used in image quality enhancement, image texture enhancement [13], image denoising [14], and image edge analysis. Among such operators [15], which are a generalization of the concept of an integer-order derivative to real order and the n-fold integral operator, are the Caputo, Erdélyi-Kober, Srivastava-Owa, and Weyl-Riesz operators [16], the Riemann-Liouville operator, and the Grünwald-Letnikov operators. Typically, the operators generate both high and low frequencies with the high frequencies characterizing a large change in pixel intensity value over a small distance including noise and edges. In contrast, the low frequency is characterized by a small change in pixel intensity value where background and texture in the image can be found [17]. This means that, in the presence of high-level noise, some of these operators proposed, if not carefully constructed, will tend to mistakenly detect fake edges.

In this paper, we present a new construction of fractional-based convolution mask for image edge analysis with equivalent complexity ($\bigcirc(mn\log(mn))$) as the standard gradient operators but with significant robustness to noise. We also show that it is able to detect edges very well as a result of the memory (kernel) function embedded in the fractional derivative. These interesting characteristic allows the operator to describe systems with memory phenomena. The paper is organized as follows: we start by reviewing some edge detection operators in Section 2. Section 3 discusses the generalized fractional calculus operator adopted for this study and subsequently in Section 4 we show how the proposed mask is constructed. In Section 5.2, we compare results from the proposed mask with two methods known to perform well. Finally, conclusions are drawn in Section 6.

2 Review of edge operators

In this section, some existing edge operators or detectors are reviewed. Edge detection is an important field in image processing and an effective edge detector is expected to reduce a large amount of data, while keeping most of the important features contained in an image. These operators are usually categorized as the gradient-based edge detectors [18–20], segmentation-based edge operators [21, 22] and the transform-based edge operators [23, 24]. The first category of edge detectors are mostly based on either first-order gradient operators or second-order operators, sometimes called Laplacians. According to [20], although higher orders are more accurate compared with first-order operators, it is relatively sensitive to noise when extracting relatively more information. For example gradient-based edge detection operators, such as the Roberts, Sobel, and Prewitts, Laplacian of Gaussian (LoG) and their improvements [25–30] uses 2-D linear filters to process vertical and horizontal edges separately in order to approximate the first-order derivative of pixel values of an image. The work of [19] also presents a classified and comparative

study of edge detection operators. In the study, the Canny operator proved to be better than LoG experimentally while LOG was better than Prewitt and Sobel in handling noisy images. A 2-D gamma distribution in the work of [18] demonstrated the efficiency of their method but, however, suffered from the drawback of big time complexity as a result of the constructed masks.

While the above operators are constructed using first- and second-order derivatives, there are other classes of edge operators based on segmentation. These methods work by partitioning the image domain into different subregions with the assumption that each subregion is homogeneous with respect to some characteristics such as intensity [21, 22, 31]. Among these operators are the Chan-Vase and Mumford-Shah methods, which separate an image into two sub domains Ω_1 and Ω_2. The sub domain Ω_1 is defined to lie inside the edge contour, C, while the other sub domain is outside C, such that the image g can be approximated by continuous functions f_1 and f_2 in Ω_1 and Ω_2, respectively. In relation to the Mumford-Shah method, this is achieved by normally minimizing the functional with respect to functions f_1, f_2, and the contour C as in equation (1):

$$\begin{aligned} E(f_1,f_2,C) = {} & \frac{1}{2}\int_{\Omega_1}(g-f_1)^2 + \frac{1}{2}\int_{\Omega_2}(g-f_2)^2 + \alpha\int_{\Omega_1}|\bigtriangledown f_1|^2 \\ & + \alpha\int_{\Omega_2}|\bigtriangledown f_2|^2 + \beta\cdot \mathrm{Length}(C). \end{aligned} \tag{1}$$

In the special case where f_1, f_2 are constant with values c_1, c_2, respectively, this formulation is simplified to the Chan-Vese segmentation method [21] according to the level set method [32]. In this case the right hand side of equation (1) becomes as follows:

$$\frac{1}{2}\int_{\Omega}\big[H(\phi)(g-c_1)^2 + \big(1-H(\phi)\big)(g-c_2)^2\big] + \beta\int_{\Omega}\big|\bigtriangledown H(\phi)\big|. \tag{2}$$

We note that the functional in (2) represents the edge contour C or the zero-level set of a Lipschitz function $\phi : \Omega \to \mathbb{R}$ where positive values of ϕ represent regions in the contour C while the negative values ϕ represent regions outside the contour. Choosing the notation $H(\cdot)$ to be the Heaviside function defined as $H(z) = 1$ for positive z and 0 otherwise, the minimizer ϕ of the functional in equation (2) gives the segmentation of the domain and the edge contours where the edges are detected from the zero-level set of ϕ.

Aside from the segmentation-based edge detection, we as well have the transform-based edge detectors. Current research in this area is the wavelet approach with box spline tight framelets in the eighth direction (B_8) as proposed by [8]. These operators have predefined properties such as compactness and smoothness, which makes it possible to approximate various edges and features better [23, 24, 33]. Nonetheless, from their study, it was concluded that the operator was efficient in tracking edges more accurately but is eight and five times more computationally expensive than that of the wavelet- and shearlet-based methods, respectively. However, it is comparable to that of the Chan-Vese method [8].

Among other edge operators used we have: the morphological gradient [34], the high-order and variable-order total variation [35], and the Mumford-Shah Green function [36] and fractal geometry-based methods [37].

3 Generalized fractional calculus operator

Fractional calculus generalizes the concept of classical calculus by taking into account non-integer orders. These classes of operators become useful when handling natural problems with memory effect since by definition these operators already possess the memory kernel [38–40] As edges need to be close and complete, based on the edge points, it is common to make use of these operators in constructing the edge map.

In this section, we provide the definitions with some preliminary concept of fractional calculus which will be the bases for the construction of a fractional mask.

Definition 3.1 (Gamma function) The gamma function, notably represented by Γ, is defined as the integral:

$$\Gamma(z) = \int_0^{+\infty} t^{z-1}e^{-t}\,dt; \quad z \in \mathbb{N} \text{ and } t \in]0, +\infty[. \tag{3}$$

From equation (3), the following properties are deduced.

$$\begin{cases} \Gamma(1) = 1, \\ \Gamma(z) = \frac{\Gamma(z+1)}{z}, \\ \Gamma(z) = (z-1)!. \end{cases} \tag{4}$$

However, for any $k \in \mathbb{Z}_-$ we have equation (5):

$$\lim_{z \to k} \Gamma(z) = \infty. \tag{5}$$

Definition 3.2 (Beta function) The beta integral is defined as in equation (6), given that $\mathrm{Re}(u) > 0$ and $\mathrm{Re}(v) > 0$ where $(u, v) \in \mathbb{N}$,

$$B(u, v) = \int_0^1 t^{u-1}(1-t)^{v-1}\,dt. \tag{6}$$

Equation (7) gives the relationship between the gamma and the beta integral,

$$B(u, v) = \frac{\Gamma(u)\Gamma(v)}{\Gamma(u+v)}, \quad \mathrm{Re}(u) > 0, \mathrm{Re}(v) > 0. \tag{7}$$

From Definition 3.1 and Definition 3.2, we define the fractional derivative and integral operator as follows in Definition 3.3 and Definition 3.4, respectively.

Definition 3.3 The fractional derivative of order α is defined, for a function $f(z)$, by

$$D_z^{\alpha} f(z) = \frac{1}{\Gamma(1-\alpha)} \frac{d}{dz} \int_0^z \frac{f(\xi)}{(z-\xi)^{\alpha}}\,d\xi; \quad 0 \le \alpha < 1, \tag{8}$$

where the function $f(z)$ is analytic in a simply connected region of the complex z-plane $\mathbb{C}$ containing the origin and the multiplicity of $(z-\xi)^{-\alpha}$ is removed by requiring $\log(z-\xi)$ to be real when $(z-\xi) > 0$.

Definition 3.4 The fractional integral of order α is defined, for a function $f(z)$, by

$$I_z^{\alpha} f(z) = \frac{1}{\Gamma(\alpha)} \int_0^z f(\xi)(z-\xi)^{\alpha-1}\, d\xi; \quad \alpha > 0, \tag{9}$$

where the function $f(z)$ is analytic in a simply connected region of the complex z-plane $\mathbb{C}$ containing the origin and the multiplicity of $(z-\xi)^{\alpha-1}$ is removed by requiring $\log(z-\xi)$ to be real when $(z-\xi) > 0$.

In [41], the formulation for the generalized fractional integral was derived by considering the natural $n \in \mathbb{N} = 1, 2, \ldots$ and the real μ in the n-fold integral of the form

$$I_z^{\alpha,\mu} f(z) = \int_0^z \xi_1^{\mu}\, d\xi_1 \int_0^{\xi_1} \xi_2^{\mu}\, d\xi_2 \cdots \int_0^{\xi_{n-1}} \xi_n^{\mu} f(\xi_n)\, d\xi_n. \tag{10}$$

Employing the Cauchy formula for the iterated integral yields equation (11),

$$\begin{aligned} \int_0^z \xi_1^{\mu}\, d\xi_1 \int_0^{\xi_1} \xi^{\mu} f(\xi)\, d\xi &= \int_0^z \xi^{\mu} f(\xi)\, d\xi \int_{\xi}^z \xi_1^{\mu}\, d\xi_1 \\ &= \frac{1}{(\mu+1)} \int_0^z \left(z^{\mu+1} - \xi^{\mu+1}\right) \xi^{\mu} f(\xi)\, d\xi. \end{aligned} \tag{11}$$

Repeating the equation (11) for $n-1$ times, equation (12) is begotten,

$$\begin{aligned} &\int_0^z \xi_1^{\mu}\, d\xi_1 \int_0^{\xi_1} \xi_2^{\mu}\, d\xi_2 \cdots \int_0^{\xi_{n-1}} \xi_n^{\mu} f(\xi_n)\, d\xi_n \\ &\quad = \frac{(\mu+1)^{1-\alpha}}{(n-1)!} \int_0^z \left(z^{\mu+1} - \xi^{\mu+1}\right)^{n-1} \xi^{\mu} f(\xi)\, d\xi, \end{aligned} \tag{12}$$

which gives rise to the fractional integral operator expressed by equation (13):

$$I_z^{\alpha,\mu} f(z) = \frac{(\mu+1)^{1-\alpha}}{\Gamma(\alpha)} \int_0^z \left(z^{\mu+1} - \xi^{\mu+1}\right)^{\alpha-1} \xi^{\mu} f(\xi)\, d\xi, \tag{13}$$

where α and $\mu \neq -1$ are real numbers and the function $f(z)$ is analytic in a simply connected region of the complex z-plane $\mathbb{C}$ containing the origin and the multiplicity of $(z^{\mu+1} - \xi^{\mu+1})^{-\alpha}$ is removed by requiring $\log(z^{\mu+1} - \xi^{\mu+1})$ to be real when $(z^{\mu+1} - \xi^{\mu+1}) > 0$. When $\mu = 0$, we arrive at the standard Riemann-Liouville fractional integral, which is used to define the Riemann-Liouville fractional derivatives.

Corresponding to the generalized fractional integral in equation (13), we define the generalized differential operator of order α by

$$D_z^{\alpha,\mu} f(z) = \frac{(\mu+1)^{\alpha}}{\Gamma(1-\alpha)} \frac{d}{dz} \int_0^z \frac{\xi^{\mu} f(\xi)}{(z^{\mu+1} - \xi^{\mu+1})^{\alpha}}\, d\xi, \quad 0 \leq \alpha < 1, \tag{14}$$

where the function $f(z)$ is analytic in a simply connected region of the complex z-plane $\mathbb{C}$ containing the origin and the multiplicity of $(z^{\mu+1} - \xi^{\mu+1})^{-\alpha}$ is removed by requiring $\log(z^{\mu+1} - \xi^{\mu+1})$ to be real when $(z^{\mu+1} - \xi^{\mu+1}) > 0$.

Theorem 3.1 *For any $f \in \mathbb{C}([a,b])$, the fractional integral operator satisfies equation* (15) *known as the semi-group property,*

$$I_a^{\alpha} I_a^{\beta} f(x) = I_a^{\alpha+\beta} f(x) \tag{15}$$

for $\alpha > 0$, $\beta > 0$

Proof By definition we have equation (16):

$$I_a^{\alpha} I_a^{\beta} f(x) = \frac{1}{\Gamma(\alpha)\Gamma(\beta)} \int_a^x \frac{dt}{(x-t)^{1-\alpha}} \int_a^t \frac{f(u)}{(t-u)^{1-\beta}}\, du, \tag{16}$$

and since $f(x) \in \mathbb{C}([a,b])$ we can by Fubini's theorem interchange the order of integration and by setting $t = u + s(x-u)$ we obtain equation (17),

$$I_a^{\alpha} I_a^{\beta} f(x) = \frac{B(\alpha,\beta)}{\Gamma(\alpha)\Gamma(\beta)} \int_a^x \frac{f(u)}{(x-u)^{1-\alpha-\beta}}\, du = I_a^{\alpha+\beta} f(x). \tag{17}$$

□

3.1 Previous methods for constructing fractional mask

In 2010, Zhang *et al.* [42] proposed the construction of fractional differential masks based on the Riemann-Liouville definition using the following Grunwald-Letnikov definition:

$$f^{(\alpha)}(t) = \sum_{k=0}^{m} \frac{f^{(k)}(a)(t-a)^{k-\alpha}}{\Gamma(k-\alpha+1)} + \frac{1}{\Gamma(m-\alpha+1)} \int_a^t (t-\tau)^{m-\alpha} f^{(m+1)}(\tau)\, d\tau. \tag{18}$$

Without loss of generality, the lower limit of the integral a was set to 0 with the duration of $s(x)$ divided into N equal shares on the interval $[0,x]$. The integral part was then rewritten to its approximate summation form and by using the difference equation, the final expression was simplified to obtain the mask.

In 2011 Yang *et al.* [9] also proposed the construction of fractional differential gradient operator. In their work, a fractional differential finite impulse filter transfer function of the form as in equation (19) was used,

$$D^{\nu}(z) = \left(\frac{1-z^{-1}}{T}\right)^{\nu}. \tag{19}$$

By rewriting this equation as $D^{\nu}(z) = \frac{1}{T^{\nu}}(1-z^{-1})^{\nu}$, the binomial series expansion was applied to obtain

$$D^{\nu}(z) = \frac{1}{T^{\nu}}\left(1 - \nu z^{-1} + \sum_{i=2}^{\infty} \frac{\nu(\nu-1)\cdots(\nu-i+1)}{i!}\left(-z^{-1}\right)^{-i}\right). \tag{20}$$

Now, expanding the summation term to the number of terms equivalent to the mask size, the fractional gradient was obtained.

Chen and Fei [43] in 2012 used the generalized Grunwald-Letnikov definition written in the form as in equation (21),

$$f^{(\alpha)}(t) = \frac{d^{\alpha} f}{dt^{\alpha}} = \lim_{h \to 0} \frac{1}{h^{\alpha}} \sum_{r=0}^{[\frac{t-a}{h}]} (-1)^{r} \binom{\alpha}{r} f(t - rh). \tag{21}$$

In their approach, the summation term was expanded in a number of terms equivalent to the size of the mask required. Finally, a single lumped mask was created and implemented using the Roberts edge detection algorithm.

In 2013, Jalab and Ibrahim [3] wrote a paper titled 'Texture enhancement for medical images based on fractional differential masks'. In the work, the Riemann-Liouville definition was rewritten in the form of Srivastava-Owa's definition as:

$$D_z^{\alpha,\mu} f(z) = \frac{(\mu+1)^{\alpha}}{\Gamma(1-\alpha+m)} \left(\frac{d}{dz}\right)^{m+1} \times \int_0^z \xi^{\mu} f(\xi) \left(z^{\mu+1} - \xi^{\mu+1}\right)^{m-\alpha} d\xi. \tag{22}$$

From this definition, the integral component was written in terms of a summation as

$$D_z^{\alpha,\mu} f(z) = \frac{(\mu+1)^{\alpha}}{\Gamma(1-\alpha+m)} \sum_{j=1}^{n} \left(\frac{d}{dz}\right)^{m+1} \times j^{\mu} f(j) \left(z^{\mu+1} - j^{\mu+1}\right)^{m-\alpha}. \tag{23}$$

Out of this expression, the function $f(z)$ was created and differentiated $m+1$ times with respect to z. The result was then expanded by setting n to be the size of the required mask. This same approach by these authors in 2013 was used in an article, 'Fractional masks based on generalized fractional differential operator for image denoising'. However, from that work, the function $f(z)$ was assumed to be a polynomial z^{ν}, which resulted in

$$D_z^{\alpha,\mu} z^{\nu} = \frac{(\mu+1)^{\alpha-1} \Gamma(\frac{\nu}{\mu+1}+1)}{\Gamma(\frac{\nu}{\mu+1}+1-\alpha)} z^{(1-\alpha)(\mu+1)+\nu-1}. \tag{24}$$

In this second approach, the degree of the polynomial defined the size of the mask.

In 2014, Gao *et al.* wrote a paper on 'Edge detection based on the Newton interpolation's fractional differentiation' and made use of a generalized Grunwald-Letnikov definition as in equation (21). In their approach, the summation term was expanded to a number of terms equivalent to the size of the mask required. Here, it was believed that these discrete points were not precise enough and needed to be improved using the Newton interpolation method.

We note that although the Riemann-Liouville definition theoretically provides an exact value for the purpose of calculus it is practically difficult when used to evaluate an integral or a derivative. Theoretically, the Riemann-Liouville definition is equivalent to the Grunwald-Letnikov definition but one question always arises as to what number of terms should be computed and summed for the Grunwald-Letnikov definition of fractional derivative to be as accurate as that of the Riemann-Liouville definition. In an attempt to answer this question Loverro *et al.* [44] used up to 171 terms to obtain an error of 1e-3%. This in a way implies that a mask size of 171×171 is required for that accuracy to be achieved. Unfortunately, the bigger the mask size, the more computationally expensive it becomes and hence this theoretical equivalence is mostly not achievable in practice.

Interestingly, the masks are extracted without evaluating the entire derivative and therefore, when carefully constructed, it can produce more desired masks results.

4 Construction of the proposed mask

Taking the Riemann-Liouville fractional integral in equation (13) at $\mu = 0$ and considering an order of $1 - \alpha$ on it, we have equation (25):

$$I_z^{1-\alpha} f(z) = \frac{1}{\Gamma(1-\alpha)} \int_0^z f(\xi)(z-\xi)^{-\alpha}\, d\xi; \quad \alpha > 0. \tag{25}$$

Putting equation (14) at $\mu = 0$ in the form as in equation (26), one observes that it contains a portion of equation (25) making it possible to write equation (26) as equation (27),

$$D_z^{\alpha} f(z) = \frac{d}{dz} \frac{1}{\Gamma(1-\alpha)} \int_0^z \frac{f(\xi)}{(z-\xi)^{\alpha}}\, d\xi; \quad 0 \le \alpha < 1 \tag{26}$$

$$= \frac{d}{dz} I_z^{1-\alpha} f(z). \tag{27}$$

Definition 4.1 Let $f(t)$ and $g(t)$ be two functions. The convolution of f and g, denoted by $f * g$, is the function on $t \ge 0$ given by

$$f * g(t) = \int_{x=0}^{t} f(x) g(t-x)\, dx. \tag{28}$$

Theorem 4.1 *Let α be a constant, and let f and g be two functions, then*

$$\int_{x=0}^{t} \big[\alpha f(x)\big] g(t-x)\, dx = \int_{x=0}^{t} f(x)\big[\alpha g(t-x)\big]\, dx = \alpha \int_{x=0}^{t} f(x) g(t-x)\, dx, \tag{29}$$

which can be written as

$$[\alpha f] * g = f * [\alpha g] = \alpha [f * g]. \tag{30}$$

If D is a differential operator and the functions f and g are analytic, then by the derivative property of a convolution we have equation (31),

$$D\big(\alpha [f * g]\big)(t) = \alpha D f(t) * g(t). \tag{31}$$

By invoking Definition 4.1, equation (25) can be written as equation (32),

$$\begin{aligned} I_z^{1-\alpha} f(z) &= \int_0^z f(\xi) \frac{(z-\xi)^{-\alpha}}{\Gamma(1-\alpha)}\, d\xi; \quad \alpha > 0, \\ &= f(z) * g(z) \\ &= g(z) * f(z) = \frac{z^{-\alpha}}{\Gamma(1-\alpha)} * f(z). \end{aligned} \tag{32}$$

Substituting the last expression of equation (32) into equation (27) and applying Theorem 4.1, we arrive at

$$D_z^{\alpha} f(z) = \frac{d}{dz}\left(\frac{z^{-\alpha}}{\Gamma(1-\alpha)} * f(z) \right) = \frac{d}{dz}\left(\frac{z^{-\alpha}}{\Gamma(1-\alpha)} \right) * f(z). \tag{33}$$

Definition 4.2 For any doublet $(n,p) \in \mathbb{N} \times \mathbb{Q} - (-1,-1)$ and for $z \in \mathbb{R}^+$, a derivative of order n of the function f such that:

$$f(z) = az^{-p} = \begin{cases} a & \text{if } z = 0 \text{ and } p = 0, \\ 0 & \text{if } z = 0 \text{ and } p \neq 0, \\ ae^{-p\ln(z)} & \text{if } z > 0 \text{ and } p \neq 0, \end{cases} \tag{34}$$

is defined by

$$\begin{aligned} \frac{d^n(ax^{-p})}{dz^n} &= a\frac{d^n z^{-p}}{dz^n} \\ &= (-1)^n \frac{a\Gamma(p+n)}{\Gamma(p)} z^{-(p+n)} \quad \text{for } p \geq 0. \end{aligned} \tag{35}$$

In order to make the generation of the mask clearer, we let $g(z) = \frac{d}{dz}(\frac{z^{-\alpha}}{\Gamma(1-\alpha)})$ from equation (32) and write it in the form shown in equation (36),

$$g(z) = \frac{1}{\Gamma(1-\alpha)} \frac{d}{dz} z^{-\alpha}, \quad 0 \leq \alpha < 1. \tag{36}$$

By direct comparison of equation (36) with the expression in Definition 4.2, we have $a = \frac{1}{\Gamma(1-\alpha)}$, $n = 1$, and $p = \alpha$, hence, by evaluation we have

$$g(z) = -\frac{\Gamma(\alpha+1)}{\Gamma(\alpha)\Gamma(1-\alpha)} z^{-(\alpha+1)}, \quad 0 \leq \alpha < 1. \tag{37}$$

Now, by literally applying these approaches to the generalized differential operator in equation (14), we obtain the following:

$$\begin{aligned} D_z^{\alpha,\mu} f(z) &\approxeq \frac{(\mu+1)^\alpha}{\Gamma(1-\alpha)} \frac{d}{dz} \left(z^{-\alpha(\mu+1)} * p(z) \right) \\ &\approxeq \frac{(\mu+1)^\alpha}{\Gamma(1-\alpha)} \frac{d}{dz} z^{-\alpha(\mu+1)} * p(z), \end{aligned} \tag{38}$$

where $p(z) = z^\mu f(z)$.

At this point it will be necessary to strip off the term z^μ in $p(z)$ to get equation (39),

$$\begin{aligned} D_z^{\alpha,\mu} f(z) &\approxeq \frac{(\mu+1)^\alpha}{\Gamma(1-\alpha)} \frac{d}{dz} \left(z^{-\alpha(\mu+1)} \times z^\mu \right) * f(z) \\ &\approxeq \frac{(\mu+1)^\alpha}{\Gamma(1-\alpha)} \frac{d}{dz} z^{-\alpha(\mu+1)+\mu} * f(z). \end{aligned} \tag{39}$$

Since α and μ are both constant parameters, it suffices that equation (35) is still applicable to equation (39), which results in equation (40):

$$g_\mu(z) \approxeq \frac{(\mu+1)^\alpha}{\Gamma(1-\alpha)} \left[-\frac{\Gamma(\alpha(\mu+1)-\mu+1)}{\Gamma(\alpha(\mu+1)-\mu)} \right] z^{-(\alpha(\mu+1)-\mu+1)}. \tag{40}$$

Definition 4.3 Given that $f(z)$ is analytic with $z \in \mathbb{R}$ and $\alpha \in \mathbb{Q}$, then the higher-ordered generalized fractional derivative operator is defined as

$$D_z^{\alpha,\mu} f(z) = \frac{(\mu+1)^\alpha}{\Gamma(1-\alpha+m)} \left(\frac{d}{dz}\right)^{m+1} \int_0^z \frac{\xi^\mu f(\xi)}{\xi^m (z^{\mu+1} - \xi^{\mu+1})^{\alpha-m}} \, d\xi, \quad m = \lfloor \alpha \rfloor. \tag{41}$$

To develop the generalized gradient edge detection mask out of equation (41) by following the previous steps, we let

$$p_m^{\alpha,\mu} = \frac{(\mu+1)^\alpha}{\Gamma(1-\alpha+m)}.$$

By concentrating on the integral part of equation (41) and expressing it in terms of the rest we arrive at equation (42) and equation (43),

$$\begin{aligned} \int_0^z \frac{\xi^\mu f(\xi)}{\xi^m (z^{\mu+1} - \xi^{\mu+1})^{\alpha-m}} \, d\xi &= \int_0^z \xi^{\mu-m} f(\xi) \left[\left(z^{\mu+1} - \xi^{\mu+1}\right)^{-(\alpha-m)} \right] d\xi \\ &= z^{\mu-m} \left(z^{\mu+1}\right)^{-(\alpha-m)} * f(z), \end{aligned} \tag{42}$$

$$\begin{aligned} D_z^{\alpha,\mu} f(z) &= p_m^{\alpha,\mu} \cdot \left(\frac{d}{dz}\right)^{m+1} \left[z^{\mu-m} \left(z^{\mu+1}\right)^{-(\alpha-m)} * f(z) \right] \\ &= p_m^{\alpha,\mu} \cdot \left(\frac{d}{dz}\right)^{m+1} z^{-[(\mu+1)(\alpha-m)+m-\mu]} * f(z) \\ &= p_m^{\alpha,\mu} \cdot \left(\frac{d}{dz}\right)^{m+1} z^{-[\alpha(\mu+1)-\mu(m+1)]} * f(z). \end{aligned} \tag{43}$$

Picking out the mask component in equation (43) and substituting it into Definition 4.2 we finally arrive at equation (44),

$$\begin{aligned} g_\mu^m(z) &= p_m^{\alpha,\mu} \cdot \left(\frac{d}{dz}\right)^{m+1} z^{-[\alpha(\mu+1)-\mu(m+1)]} \\ &= p_m^{\alpha,\mu} \cdot \left((-1)^{m+1} \frac{\Gamma[\alpha(\mu+1) + (m+1)(1-\mu)]}{\Gamma[\alpha(\mu+1) - \mu(m+1)]} z^{-(\alpha(\mu+1)+(m+1)(1-\mu))} \right) \\ &= \frac{(\mu+1)^\alpha}{\Gamma(1-\alpha+m)} \left((-1)^{m+1} \frac{\Gamma[\alpha(\mu+1) + (m+1)(1-\mu)]}{\Gamma[\alpha(\mu+1) - \mu(m+1)]} z^{-(\alpha(\mu+1)+(m+1)(1-\mu))} \right). \end{aligned} \tag{44}$$

4.1 Edge mask representation

Since the Riemann-Liouville fractional derivative mask is the desired operator of interest for our image edge analysis, equation (36) is considered. However, this equation cannot be directly applied to an image in its one-dimensional form and needs to be transformed into two dimensions. This is achieved by letting

$$z \to \sqrt{x^2 + y^2}. \tag{45}$$

Substituting this expression into equation (4), we obtain equation (46) and equation (47), which are the gradient operators in the direction of x and y, respectively, in two-

Table 1 Proposed *x*-directional fractional mask

$\frac{2\alpha\sqrt{8^{\alpha}}}{8\Gamma(1-\alpha)}$	$\frac{\alpha\sqrt{5^{\alpha}}}{5\Gamma(1-\alpha)}$	0	$\frac{-\alpha\sqrt{5^{\alpha}}}{5\Gamma(1-\alpha)}$	$\frac{-2\alpha\sqrt{8^{\alpha}}}{8\Gamma(1-\alpha)}$
$\frac{2\alpha\sqrt{5^{\alpha}}}{5\Gamma(1-\alpha)}$	$\frac{\alpha\sqrt{2^{\alpha}}}{2\Gamma(1-\alpha)}$	0	$\frac{-\alpha\sqrt{2^{\alpha}}}{2\Gamma(1-\alpha)}$	$\frac{-2\alpha\sqrt{5^{\alpha}}}{5\Gamma(1-\alpha)}$
$\frac{2\alpha\sqrt{4^{\alpha}}}{4\Gamma(1-\alpha)}$	$\frac{\alpha}{\Gamma(1-\alpha)}$	0	$\frac{-\alpha}{\Gamma(1-\alpha)}$	$\frac{-2\alpha\sqrt{4^{\alpha}}}{4\Gamma(1-\alpha)}$
$\frac{2\alpha\sqrt{5^{\alpha}}}{5\Gamma(1-\alpha)}$	$\frac{\alpha\sqrt{2^{\alpha}}}{2\Gamma(1-\alpha)}$	0	$\frac{-\alpha\sqrt{2^{\alpha}}}{2\Gamma(1-\alpha)}$	$\frac{-2\alpha\sqrt{5^{\alpha}}}{5\Gamma(1-\alpha)}$
$\frac{2\alpha\sqrt{8^{\alpha}}}{8\Gamma(1-\alpha)}$	$\frac{\alpha\sqrt{5^{\alpha}}}{5\Gamma(1-\alpha)}$	0	$\frac{-\alpha\sqrt{5^{\alpha}}}{5\Gamma(1-\alpha)}$	$\frac{-2\alpha\sqrt{8^{\alpha}}}{8\Gamma(1-\alpha)}$

Table 2 Proposed *y*-directional fractional mask

$\frac{2\alpha\sqrt{8^{\alpha}}}{8\Gamma(1-\alpha)}$	$\frac{2\alpha\sqrt{5^{\alpha}}}{5\Gamma(1-\alpha)}$	$\frac{2\alpha\sqrt{4^{\alpha}}}{4\Gamma(1-\alpha)}$	$\frac{2\alpha\sqrt{5^{\alpha}}}{5\Gamma(1-\alpha)}$	$\frac{2\alpha\sqrt{8^{\alpha}}}{8\Gamma(1-\alpha)}$
$\frac{\alpha\sqrt{5^{\alpha}}}{5\Gamma(1-\alpha)}$	$\frac{\alpha\sqrt{2^{\alpha}}}{2\Gamma(1-\alpha)}$	$\frac{\alpha}{\Gamma(1-\alpha)}$	$\frac{\alpha\sqrt{2^{\alpha}}}{2\Gamma(1-\alpha)}$	$\frac{\alpha\sqrt{5^{\alpha}}}{5\Gamma(1-\alpha)}$
0	0	0	0	0
$\frac{-\alpha\sqrt{5^{\alpha}}}{5\Gamma(1-\alpha)}$	$\frac{-\alpha\sqrt{2^{\alpha}}}{2\Gamma(1-\alpha)}$	$\frac{-\alpha}{\Gamma(1-\alpha)}$	$\frac{-\alpha\sqrt{2^{\alpha}}}{2\Gamma(1-\alpha)}$	$\frac{-\alpha\sqrt{5^{\alpha}}}{5\Gamma(1-\alpha)}$
$\frac{-2\alpha\sqrt{8^{\alpha}}}{8\Gamma(1-\alpha)}$	$\frac{-2\alpha\sqrt{5^{\alpha}}}{5\Gamma(1-\alpha)}$	$\frac{-2\alpha\sqrt{4^{\alpha}}}{4\Gamma(1-\alpha)}$	$\frac{-2\alpha\sqrt{5^{\alpha}}}{5\Gamma(1-\alpha)}$	$\frac{-2\alpha\sqrt{8^{\alpha}}}{8\Gamma(1-\alpha)}$

dimensional (2D) form,

$$\begin{aligned}\Theta_x(x,y) &= \frac{1}{\Gamma(1-\alpha)}\frac{d}{dx}\left(x^2+y^2\right)^{-\alpha/2}, \quad 0 \le \alpha < 1\\ &= -\frac{\alpha\cdot x}{\Gamma(1-\alpha)}\left(x^2+y^2\right)^{-\alpha/2-1}, \end{aligned} \tag{46}$$

$$\begin{aligned}\Theta_y(x,y) &= \frac{1}{\Gamma(1-\alpha)}\frac{d}{dy}\left(x^2+y^2\right)^{-\alpha/2}, \quad 0 \le \alpha < 1\\ &= -\frac{\alpha\cdot y}{\Gamma(1-\alpha)}\left(x^2+y^2\right)^{-\alpha/2-1}. \end{aligned} \tag{47}$$

Since equation (46) and equation (47) will be applied to a digital image which is in the discrete form, we have to rewrite them in a more presentable way as in equation (48) and equation (49) in order to construct the mask in Tables 1 and 2,

$$\Theta_x(x_i,y_i) = -\frac{\alpha\cdot x_i}{\Gamma(1-\alpha)}\left(x_i^2+y_i^2\right)^{-\alpha/2-1}, \tag{48}$$

$$\Theta_y(x_i,y_i) = -\frac{\alpha\cdot y_i}{\Gamma(1-\alpha)}\left(x_i^2+y_i^2\right)^{-\alpha/2-1}, \tag{49}$$

where $-m \le i \le m$ and $-n \le j \le n$ with $(2m+1)\times(2n+1)$ being the mask (grid) size for all $m,n \ge 1$ and α a constant parameter. To avoid making the filter error too large and also to make a fair comparison with other masks, we construct a 5×5 fractional gradient mask.

4.2 Performance metric of proposed mask

In order to justify the performance of the proposed mask, we use the following standard measures as detailed in the subsections below.

4.2.1 Mean squared error

To measure the associated error based on quality, the mean squared error (MSE) between two $M\times N$ images, I_A and I_B, is given by

$$\mathrm{MSE} = \frac{1}{MN}\sum_{i=1}^{M}\sum_{j=1}^{N}\left(I_A(i,j)-I_B(i,j)\right)^2. \tag{50}$$

4.2.2 Peak signal-to-noise ratio

The peak signal-to-noise ratio (PSNR) is basically the proportion of the power of the maximum possible intensity value in an image based on sample per bits to its mean square error expressed in logarithmic decibel scale. The greater the PSNR value, the better the image quality and noise suppression. The PSNR is calculated as follows:

$$\mathrm{PSNR} = 10 \times \log_{10}\left(\frac{\|I\|_\infty{}^2}{MSE}\right). \tag{51}$$

4.2.3 Structural similarity index

The structural similarity index measure (SSIM) is a method for measuring the similarity between two images [1]. The SSIM index is a full reference metric for measuring image quality using an initial noise-free-image as reference. The following formulation of SSIM index was used in this study:

$$\mathrm{SSIM}(A,B) = \frac{(2\mu_A\mu_B + C_1)(2\sigma_{AB} + C_2)}{(\mu_A^2 + \mu_B^2 + C_1)(\sigma_A^2 + \sigma_B^2 + C_2)}, \tag{52}$$

where μ_A and μ_B are the estimated mean intensity along the A, B directions and σ_A and σ_B are the standard deviations, respectively. σ_{AB} was estimated as

$$\sigma_{AB} = \left(\frac{1}{N-1}\sum_{i=1}^{N}(A_i - \mu_A)(B_i - \mu_B)\right), \tag{53}$$

where $C_1 = (K_1L)^2$ and $C_2 = (K_2L)^2$ are constants with $K_1, K_2 \ll 1$ being relatively small and constant and L being the dynamic range of the pixel values (normally 255). The resultant SSIM index is a decimal value between −1 and 1 and has a value of 1 in the case of two identical sets of images.

5 Result and analysis of proposed mask

5.1 Data source

The dataset used for this study was acquired from the Live for Image & Video Engineering (LIVE) database [45] and OsiriX imaging software, which is an advanced open-source PACS workstation DICOM viewer. The test sample as shown in Figure 1 was selected to check the scalability of the algorithm to standard imaging issues with the methods existing in the literature.

During image acquisition, the resulting image is affected with various artifact regarded as noise. However, these noises are not expected to be visible to all algorithms during edge detection since it influences the final output of the edge map. Figure 2 gives a sample of some images distorted with Gaussian white noise of standard deviation 15.

5.2 Numerical experiments

This section consists of three sets of experimental results. In Section 5.2.1, we compared the proposed fractional edge detector with some selected edge detectors: Canny [46], and Tiansi [9], using the mean square error and the peak signal-to-noise ratio. In Section 5.2.2, we also tested the performance of the proposed method in detecting edges of an images

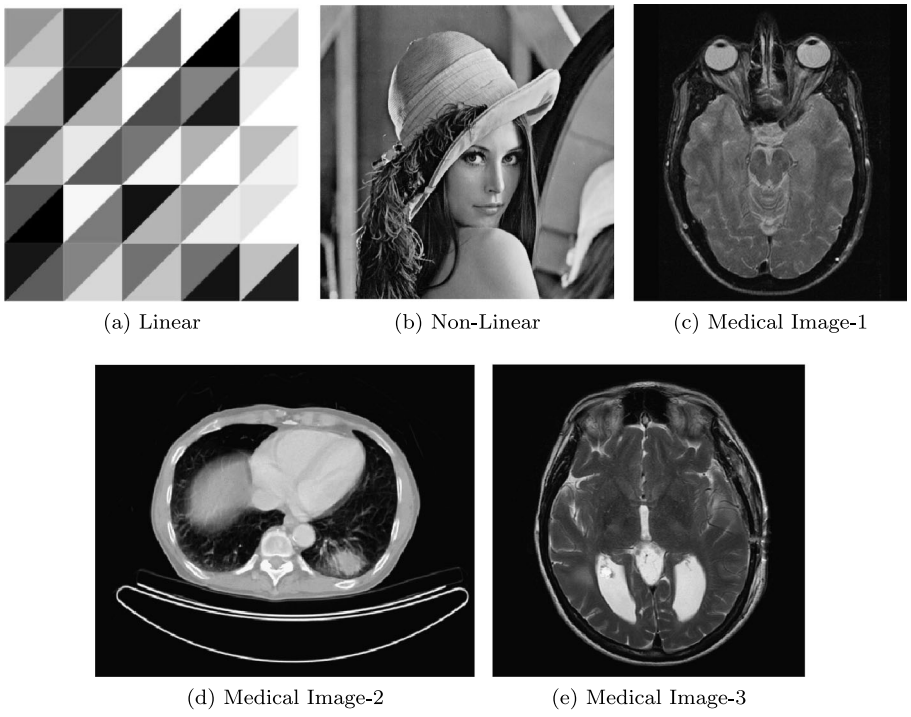

(a) Linear (b) Non-Linear (c) Medical Image-1

(d) Medical Image-2 (e) Medical Image-3

Figure 1 Original sample images for testing comparison.

(a) Linear (b) Non-Linear (c) Medical

Figure 2 Sample noisy image at standard deviation = 15.

under various noise conditions using the structure similarity index measure, and in Section 5.2.3 we focused on object segmentation of some selected Medical image. The choice of these methods is based on earlier studies like [9, 18, 19, 41].

5.2.1 Experimental result 1: *performance test*

In this section, we demonstrate the general performance of our proposed mask using different fractional orders of the differential operator. Here, the peak signal-to-noise ratio (PSNR) and the mean square error (MSE) of the edge information are extracted during the implementation of the fractional mask and Canny. These algorithms are applied to the images 2 tagged as Linear, Non-linear, and Medical image-1. It is interesting to note that these algorithms behave differently with varying mask size. In this work, a mask of size 3×3, 5×5, 7×7, and 9×9 is tested on each image for a fair comparison. It is ex-

Table 3 Proposed method with Canny using a 3 × 3 mask size

Method	Linear image		Non-linear image		Medical image	
	MSE	PSNR	MSE	PSNR	MSE	PSNR
CANNY	0.2571	5.8995	0.3012	5.2111	0.3178	4.9782
PRO $\alpha = 0.1$	0.2476	6.0633	0.2945	5.3086	**0.2888**	**5.3935**
PRO $\alpha = 0.2$	0.2479	6.0564	**0.2943**	**5.3118**	0.2892	5.3877
PRO $\alpha = 0.3$	0.2471	6.0718	0.2945	5.3087	0.2907	5.3650
PRO $\alpha = 0.4$	0.2476	6.0632	0.2947	5.3059	0.2911	5.3597
PRO $\alpha = 0.5$	**0.2465**	**6.0817**	0.2953	5.2973	0.2916	5.3516
PRO $\alpha = 0.6$	0.2476	6.0623	0.2957	5.2915	0.2922	5.3432
PRO $\alpha = 0.7$	0.2480	6.0558	0.2960	5.2864	0.2940	5.3165
PRO $\alpha = 0.8$	0.2475	6.0637	0.2960	5.2874	0.2942	5.3132
PRO $\alpha = 0.9$	0.2478	6.0588	0.2962	5.2845	0.2957	5.2919

Table 4 Proposed method with Canny using a 7 × 7 mask size

Method	Linear image		Non-linear image		Medical image	
	MSE	PSNR	MSE	PSNR	MSE	PSNR
CANNY	0.1296	8.8727	0.1025	9.8911	0.1462	8.3508
PRO $\alpha = 0.1$	**0.0308**	**15.1136**	**0.0509**	**12.9351**	**0.0761**	**11.1853**
PRO $\alpha = 0.2$	0.0324	14.8995	0.0512	12.9059	0.0826	10.8284
PRO $\alpha = 0.3$	0.0349	14.5731	0.0525	12.8024	0.0857	10.6699
PRO $\alpha = 0.4$	0.0386	14.1369	0.0540	12.6788	0.0878	10.5664
PRO $\alpha = 0.5$	0.0412	13.8542	0.0559	12.5255	0.0906	10.4278
PRO $\alpha = 0.6$	0.0441	13.5601	0.0581	12.3555	0.0929	10.3218
PRO $\alpha = 0.7$	0.0459	13.3825	0.0604	12.1876	0.0966	10.1494
PRO $\alpha = 0.8$	0.0529	12.7643	0.0635	11.9705	0.0999	10.0030
PRO $\alpha = 0.9$	0.0571	12.4334	0.0647	11.8881	0.1039	9.8346

pected that the higher the value of the PSNR, the better the edge information extracted. In contrast, the lower the MSE value, the closer the edge information extracted is, to the true and actual edge map.

Observation on a 3×3 *mask*

From Table 3, we observed that our mask on a whole, performed better as compared to the Canny algorithm at all image types. In particular, at fractional order of $\alpha = 0.5$ for the proposed mask gave the best measure of quality on the Linear image, $\alpha = 0.2$ on the Non-linear image and $\alpha = 0.1$ on the Medical image. Although the other α values were not considered due to comparatively lower performances, we note that they were all above the Canny performance values, which confirms the significant strength a fractional mask possesses over classical methods.

Observation on a 7×7 *mask*

With the 7×7 mask, the proposed method again at all orders of α performed better than the Canny approach. However, $\alpha = 0.1$ stood out as the most efficient at various image levels. The results in Table 4 indicates that the fractional mask has a linear relationship with the α values, and the higher the fractional order, the higher the MSE value and the lower the PSNR value at all instances of the images used. Although generally the choice of an appropriate order or α value for the mask may be difficult to decide on, this relation allows us to choose $\alpha = 0.1$ over the rest and in fact this choice appears to be quite consistent for the subsequent masks.

Table 5 Proposed method and Tiansi with Canny using a 5 × 5 mask size

Method	Linear image		Non-linear image		Medical image	
	MSE	PSNR	MSE	PSNR	MSE	PSNR
CANNY	0.2266	6.4483	0.2670	5.7342	0.2393	6.2102
PRO $\alpha = 0.1$	**0.1580**	**8.0138**	0.1607	7.9402	0.1538	8.1298
PRO $\alpha = 0.2$	0.1594	7.9754	0.1659	7.8009	0.1594	7.9746
PRO $\alpha = 0.3$	0.1651	7.8232	0.1730	7.6206	0.1669	7.7753
PRO $\alpha = 0.4$	0.1718	7.6488	0.1784	7.4856	0.1732	7.6155
PRO $\alpha = 0.5$	0.1759	7.5465	0.1858	7.3088	0.1786	7.4805
PRO $\alpha = 0.6$	0.1806	7.4329	0.1945	7.1100	**0.1419**	**8.4810**
PRO $\alpha = 0.7$	0.1849	7.3301	0.2003	6.9842	0.1462	8.3519
PRO $\alpha = 0.8$	0.1889	7.2382	**0.1591**	**7.9826**	0.1502	8.2345
PRO $\alpha = 0.9$	0.1930	7.1440	0.1655	7.8130	0.1573	8.0340
TIA $\alpha = 0.1$	0.1702	7.6899	0.1765	7.5337	0.1686	7.7307
TIA $\alpha = 0.2$	0.1764	7.5344	0.1825	7.3883	0.1762	7.5388
TIA $\alpha = 0.3$	0.1835	7.3626	0.1901	7.2093	0.1842	7.3468
TIA $\alpha = 0.4$	0.1896	7.2214	0.1981	7.0312	0.1484	8.2843
TIA $\alpha = 0.5$	0.1957	7.0833	0.2081	6.8166	0.1542	8.1201
TIA $\alpha = 0.6$	0.2035	6.9149	0.2171	6.6326	0.1640	7.8520
TIA $\alpha = 0.7$	0.2140	6.6951	0.1865	7.2938	0.1785	7.4829
TIA $\alpha = 0.8$	0.1681	7.7450	0.2008	6.9718	0.1922	7.1620
TIA $\alpha = 0.9$	0.1830	7.3749	0.2159	6.6569	0.2077	6.8246

Table 6 Proposed method with Canny using a 9 × 9 mask size

Method	Linear image		Non-linear image		Medical image	
	MSE	PSNR	MSE	PSNR	MSE	PSNR
CANNY	0.0810	10.9149	0.0762	11.1777	0.1148	9.4000
PRO $\alpha = 0.1$	0.0142	18.4743	**0.0347**	**14.5988**	**0.0532**	**12.7443**
PRO $\alpha = 0.2$	**0.0140**	**18.5449**	0.0360	14.4375	0.0543	12.6515
PRO $\alpha = 0.3$	0.0143	18.4441	0.0368	14.3451	0.0558	12.5306
PRO $\alpha = 0.4$	0.0146	18.3638	0.0381	14.1945	0.0568	12.4597
PRO $\alpha = 0.5$	0.0146	18.3684	0.0400	13.9797	0.0588	12.3071
PRO $\alpha = 0.6$	0.0149	18.2827	0.0417	13.7940	0.0605	12.1796
PRO $\alpha = 0.7$	0.0193	17.1344	0.0436	13.6057	0.0702	11.5370
PRO $\alpha = 0.8$	0.0210	16.7856	0.0448	13.4854	0.0724	11.4034
PRO $\alpha = 0.9$	0.0227	16.4349	0.0462	13.3500	0.0754	11.2258

Observation on a 5×5 *mask*

At this section, three algorithms were considered; Canny, Tiansi, and our proposed method. The Tiansi and the proposed method are fractional-based, while Canny is ordinary or classically based. The Tiansi [9] algorithm in this work was used to validate whether the proposed method is indeed efficient or not and also to confirm that the use of fractional calculus in modern signal and image processing is in general efficient. A mask size of 5 was used for this analysis, since Tiansi's experiments were done using only mask size of 5. From Table 5, we have three different α values depending on the image choice. It is clear that $\alpha = 0.1$ is a good choice for the Linear image, $\alpha = 0.8$ for a Non-linear image, and $\alpha = 0.6$ for a Medical image using the proposed method. Although the Tiansi mask did not do as well as the proposed method, we confirm that it performed better than Canny at $\alpha = 0.1$ for both Linear and Non-linear images and $\alpha = 0.4$ for the Medical image.

Observation on a 9×9 *mask*

One will expect that a mask size of 9×9 will perform better or at least behave the same as that of the 7×7 mask. Unfortunately, this is not so as observed from Table 6 and

many other experiments we conducted. It appears that the mask size varies with different fractional-order values in order to obtain the desired quality and efficient edge maps. The Linear image had an appropriate edge estimation at $\alpha = 0.2$, while the Nonlinear and the Medical images were at $\alpha = 0.1$ and they again were performing better than Canny.

General remarks

From all the observations made on 3×3, 5×5, 7×7, and 9×9 it was clear that increasing the mask size irrespective of the image type or the derivative operator increases the performance metric value. This is due to the choice of the standard deviation, σ in the Gaussian filter which has a direct influence on the size of the mask. Using the same σ value in the Gaussian filter on all three methods also meant that smoothing techniques were the same and therefore should not affect the results. The only part which was varied was the choice of the mask.

5.2.2 Experimental result 2: *noise immunity*

In practice, during image acquisition, one will often expect that the resulting image will be contaminated with some uncontrolled features. These features, depending on what you want, may be neglected and no further processing will be required. But obviously an algorithm's ability to handle these features will make it invariant and robust making its implementation useful. Among some of these features are:

(1) Gauss: Gaussian white noise with constant mean and variance.
(2) S & P: salt & pepper noise.
(3) localvar: zero mean Gaussian white noise with an intensity dependent variance
(4) speckle: speckle or Multiplicative noise.
(5) Poisson: shot noise.
(6) motion: Motion Blur (blurry pixels).
(7) erosion: morphological erosion.
(8) dilation: morphological dilation.
(9) jpg compression blocking effect: compression artifact.

However, in this paper, only four (1), (2), (4), (6) out of the above mentioned were considered, since they are the most often occurring contamination; they are likely to affect our case. In the next subsections, we will discuss in detail the behaviors of the Canny and our proposed methods with various mask sizes at varying noise types. Here, the performance metric used is the structural similarity index [47], which generally has the capability to measure how much an image is distorted after being made to go through various noise types. The higher the value of the similarity index, the higher the similarity of the recovered image to the expected image.

Noise immunity with 3×3 *mask*

From Tables 7 and 8, it is clear that each image with a particular noise type having an increase in the noise level leads to a decay in the performance value. In applying a 3×3 mask to the Linear image, the proposed method experienced a sharp decay from noise level 30 to 45. Nonetheless, the proposed method performed relatively better for the Nonlinear and Medical images under Motion Blur and Gaussian white noise. Generally for a

Table 7 Noise immunity with 3 × 3 Canny mask at varying standard deviations (Noise SD)

Noise type	Noise SD	20	25	30	35	40	45
Motion	Linear image	0.7536	0.7094	0.6124	0.6013	0.5848	0.5910
	Non-linear image	0.5785	0.4246	0.3709	0.3618	0.3529	0.3386
	Medical image	0.6707	0.4566	0.3815	0.3785	0.3774	0.3681
Gauss	Linear image	0.1081	0.0892	0.0777	0.0655	0.0563	0.0555
	Non-linear image	0.0861	0.0650	0.0535	0.0431	0.0375	0.0331
	Medical image	0.0426	0.0361	0.0235	0.0208	0.0155	0.0129
S & P	Linear image	0.7103	0.5708	0.4780	0.4003	0.3392	0.2523
	Non-linear image	0.6731	0.5846	0.4842	0.4230	0.3655	0.2897
	Medical image	0.7241	0.6630	0.5875	0.4919	0.3687	0.3162
Speckle	Linear image	0.2618	0.2416	0.2266	0.2132	0.2021	0.1947
	Non-linear image	0.2303	0.1966	0.1641	0.1513	0.1338	0.1147
	Medical image	0.5528	0.5280	0.4972	0.4614	0.4571	0.4373

Table 8 Noise immunity with a 3 × 3 proposed mask at $\alpha = 0.5$ and varying standard deviations (Noise SD)

Noise type	Noise SD	20	25	30	35	40	45
Motion	Linear image	0.7788	0.7137	0.6056	0.5839	0.5704	0.5569
	Non-linear image	0.6364	0.4761	0.4056	0.3939	0.3847	0.3647
	Medical image	0.7040	0.5028	0.4251	0.4174	0.4127	0.4025
Gauss	Linear image	0.1249	0.1007	0.0893	0.0785	0.0686	0.0604
	Non-linear image	0.1033	0.0793	0.0665	0.0559	0.0480	0.0430
	Medical	0.0593	0.0451	0.0336	0.0274	0.0199	0.0178
S & P	Linear image	0.6006	0.5064	0.4258	0.3549	0.3100	0.2409
	Non-linear image	0.6909	0.5616	0.4560	0.3974	0.3267	0.2580
	Medical image	0.7545	0.6764	0.5963	0.4477	0.3870	0.2940
Speckle	Linear image	0.2526	0.2276	0.2298	0.2117	0.2060	0.1967
	Non-linear image	0.2887	0.2305	0.2005	0.1915	0.1629	0.1436
	Medical image	0.6337	0.5858	0.5691	0.5267	0.5125	0.4960

mask size of 3, the Canny method exhibited an alternating performance with the proposed method.

Noise immunity with 7×7 *mask*

Observation of the noise immunity in Tables 9 and 10 reveals that the proposed method at all times performed better than the Canny technique, except for the Medical image when salt & pepper noise was applied to the image.

Noise immunity with 9×9 *mask*

The structural similarity index as shown in Tables 11 and 12 using a mask size of 9×9 indicates that our proposed method once again performs better for all images at all noise types with varying noise level except for salt & pepper noise, which lagged behind that of Canny. Instead an alternating performance was noticed. Due to this alternating characteristic of Canny and our proposed method on Medical images under such noise, one cannot conclude that the proposed method is efficient compared to Canny and vise versa. Nevertheless, by swapping to the 3×3 mask during, we can satisfactorily say that the proposed method in general performs better than the Canny method. In situations where a 3×3 mask is exclusively required, then 50% of both methods works better depending on the noise type and the image category. Finally, we compared all the three methods in the next section using a 5×5 mask size for a more conclusive remark.

Table 9 Noise immunity with a 7 × 7 Canny mask at varying standard deviations (Noise SD)

Noise type	Noise SD	20	25	30	35	40	45
Motion	Linear image	0.9770	0.9352	0.9112	0.8528	0.7886	0.7685
	Non-linear image	0.8399	0.7029	0.5816	0.5188	0.4836	0.4618
	Medical image	0.8096	0.6450	0.5414	0.5034	0.4873	0.4756
Gauss	Linear image	0.3329	0.2984	0.1984	0.2002	0.1816	0.1355
	Non-linear image	0.2168	0.1610	0.1409	0.1130	0.0946	0.0866
	Medical image	0.3416	0.2301	0.1167	0.1014	0.0668	0.0595
S & P	Linear image	0.7577	0.6590	0.5930	0.5193	0.4242	0.3738
	Non-linear image	0.7300	0.6223	0.5186	0.4388	0.3857	0.3127
	Medical image	0.6902	0.5847	0.5017	0.3985	0.3274	0.2593
Speckle	Linear image	0.5638	0.4109	0.4196	0.3537	0.3592	0.3213
	Non-linear image	0.6205	0.4995	0.4910	0.4148	0.3456	0.3378
	Medical image	0.7696	0.7213	0.7005	0.6748	0.6673	0.6574

Table 10 Noise immunity with a 7 × 7 proposed mask at $\alpha = 0.5$ at varying standard deviations (Noise SD)

Noise type	Noise SD	20	25	30	35	40	45
Motion	Linear image	0.9820	0.9540	0.9259	0.8792	0.8204	0.7992
	Non-linear image	0.8665	0.7562	0.6426	0.5662	0.5219	0.4961
	Medical image	0.8466	0.7085	0.5900	0.5357	0.5082	0.4939
Gauss	Linear image	0.6136	0.3837	0.3749	0.2832	0.2750	0.2799
	Non-linear image	0.5000	0.3616	0.2218	0.1723	0.1367	0.1275
	Medical image	0.5370	0.3380	0.3544	0.1866	0.1445	0.1009
S & P	Linear image	0.8089	0.7549	0.6689	0.6732	0.5958	0.4860
	Non-linear image	0.8150	0.7181	0.6169	0.5534	0.4522	0.4559
	Medical image	0.6529	0.5854	0.4799	0.3947	0.3259	0.2649
Speckle	Linear image	0.7800	0.6257	0.6336	0.4921	0.4228	0.4460
	Non-linear image	0.7456	0.7243	0.6520	0.5742	0.5087	0.4310
	Medical image	0.7720	0.7466	0.7289	0.7109	0.6961	0.6829

Table 11 Noise immunity with a 9 × 9 Canny mask at varying standard deviations (Noise SD)

Noise type	Noise SD	20	25	30	35	40	45
Motion	Linear image	0.9714	0.9355	0.9083	0.8639	0.7971	0.7770
	Non-linear image	0.8716	0.7344	0.6140	0.5439	0.5036	0.4792
	Medical image	0.8199	0.6667	0.5618	0.5152	0.4919	0.4815
Gauss	Linear image	0.4364	0.2718	0.2716	0.2771	0.2089	0.1944
	Non-linear image	0.3338	0.2347	0.1542	0.1469	0.1256	0.1021
	Medical image	0.4525	0.2374	0.1634	0.1323	0.1140	0.0881
S & P	Linear image	0.7592	0.6748	0.6125	0.5529	0.4473	0.4384
	Non-linear image	0.7285	0.6679	0.5631	0.4614	0.4139	0.3344
	Medical image	0.6997	0.5756	0.4879	0.4012	0.3158	0.2577
Speckle	Linear image	0.6689	0.4865	0.5035	0.4113	0.4316	0.3536
	Non-linear image	0.6958	0.5763	0.5672	0.4927	0.3948	0.3511
	Medical image	0.7557	0.7328	0.7107	0.6896	0.6820	0.6588

Noise immunity with 5×5 *mask*

In this section, all the three methods were compared in graphical form for clearer and distinctive observation. These methods were made to undergo all the four selected noise type at six different noise level for each test image. Each graph contains three subplots for the Linear, Non-linear, and the Medical image. Each subplot also has three plots with the continuous blue line for Canny, red short dashed discontinuous line for the Proposed and the black continuous line with black asterisk markers for Tiansi. Figure 3 is a plot of SSIM

Table 12 Noise immunity with 9 × 9 proposed mask at $\alpha = 0.5$ at varying standard deviations (Noise SD)

Noise type	Noise SD	20	25	30	35	40	45
Motion	Linear image	0.9818	0.9493	0.9270	0.8973	0.8447	0.8151
	Non-linear image	0.9098	0.8058	0.7038	0.6222	0.5671	0.5380
	Medical	0.8805	0.7732	0.6670	0.6031	0.5667	0.5427
Gauss	Linear image	0.8422	0.6467	0.6009	0.4269	0.4777	0.3587
	Non-linear image	0.6410	0.5999	0.4123	0.3266	0.2665	0.1951
	Medical image	0.6285	0.5280	0.4705	0.3381	0.2510	0.2579
S & P	Linear image	0.9254	0.8855	0.8496	0.7843	0.7707	0.7043
	Non-linear image	0.8621	0.8072	0.7358	0.6759	0.5891	0.6016
	Medical	0.6925	0.5735	0.4810	0.3943	0.4067	0.3767
Speckle	Linear image	0.9186	0.8753	0.8085	0.6825	0.5964	0.6200
	Non-linear image	0.8521	0.8050	0.7481	0.6977	0.6382	0.5735
	Medical image	0.8218	0.7981	0.7731	0.7530	0.7426	0.7194

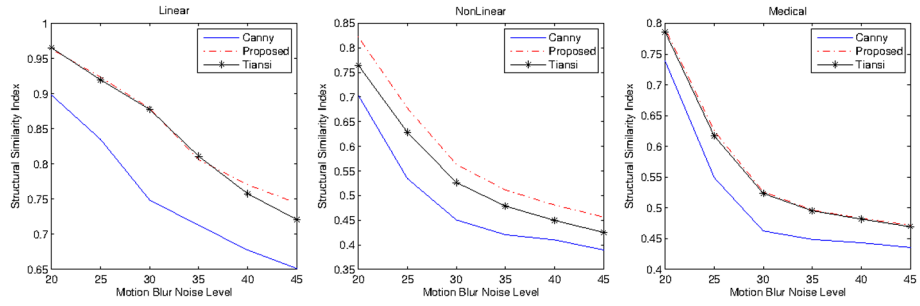

Figure 3 Effect of operators on Motion Blur noise.

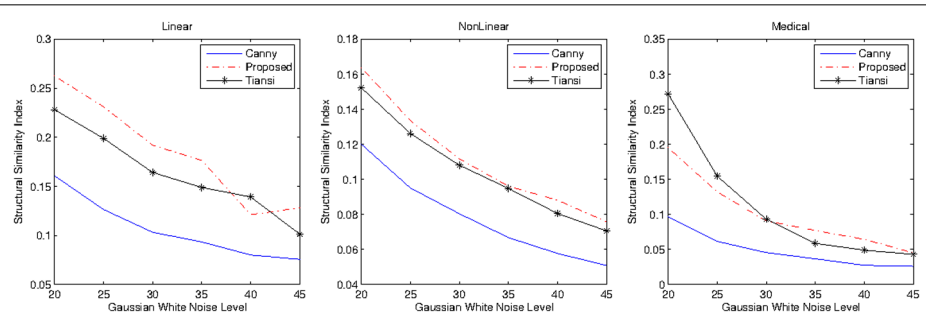

Figure 4 Effect of operators on Gaussian noise.

with Motion Blur noise, Figure 4 is a plot of SSIM with Gaussian white noise, Figure 5 is a plot of SSIM with salt & pepper noise, while the final block, Figure 6, is a plot of SSIM with speckle noise. We note that Canny's method consistently performed relatively better with salt & pepper noise immunity. However, both the proposed method and the Tiansi method generally handle the respective errors much better than that of Canny with the proposed method slightly doing better than that of Tiansi. This was quite clear when performing the segmentation procedure on the selected Medical images.

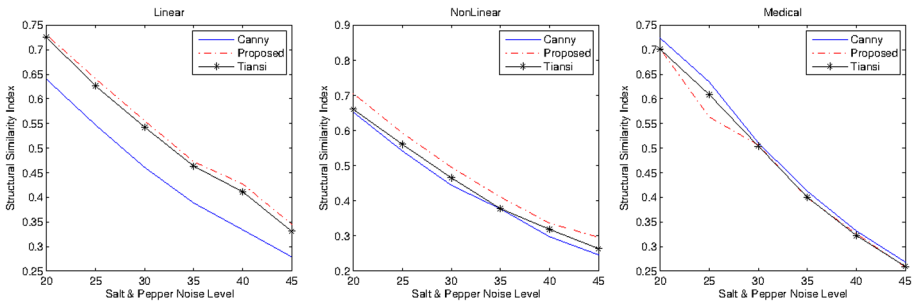

Figure 5 Effect of operators on salt & pepper noise.

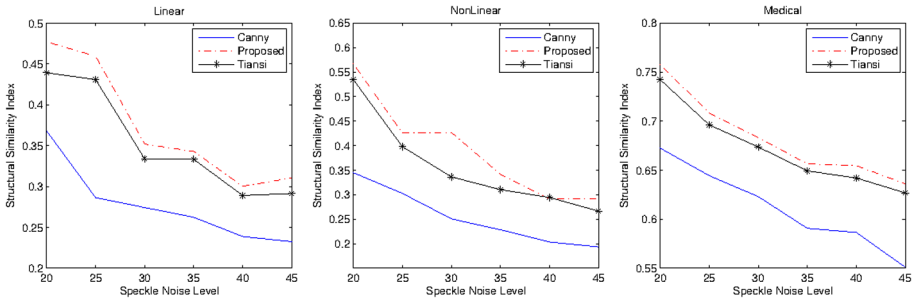

Figure 6 Effect of operators on speckle noise.

5.2.3 Experimental result 3: *segmentation*

One of the most important tasks in Medical image analysis is segmentation, which is the process of partitioning an image into a set of distinct regions, which are different in some important qualitative or quantitative way. It therefore becomes a critical intermediate step in all high-level object recognition tasks, especially in computer assisted imagery. To test the proposed method in this context, three standard medical test images were selected and their results compared to that of Canny. The Single Seed Region Growing algorithm was employed at this stage for the segmentation based on the output of the edge maps generated by Canny and the proposed method. A mask size of 9×9 was used for this purpose.

Segmentation on Medical image-1

From Figure 7, you will notice two colors, green and red. The green is meant for interior boundaries, while the red is meant for exterior boundaries. The focus of this image is for the segmentation to extract only one region of interest and that is the shape to the right. Hence it is expected that only one boundary could seen on the image. An attempt with the Canny method failed by extraction of three main boundaries with some isolated objects as boundaries. The same was the case for our proposed method at $\alpha = 0.1, 0.2,$ and 0.3, however, from $\alpha = 0.4$ to 0.9, the desired region of interest was achieved.

Segmentation on Medical image-2

With regard to the second image (see Figure 8), we expected the methods to extract four regions of interest. However, using Canny's method, three out of four regions were extracted. On testing our proposed method on the same image, $\alpha = 0.1$ and 0.2 extracted

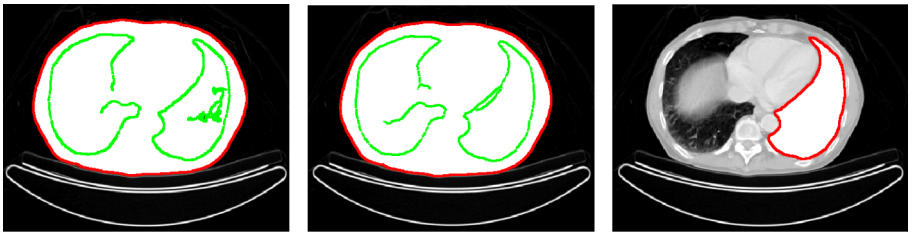

(a) Canny (b) Proposed $\alpha = 0.1$ (c) Proposed $\alpha = 0.2$

Figure 7 Segmentation using Medical image-1.

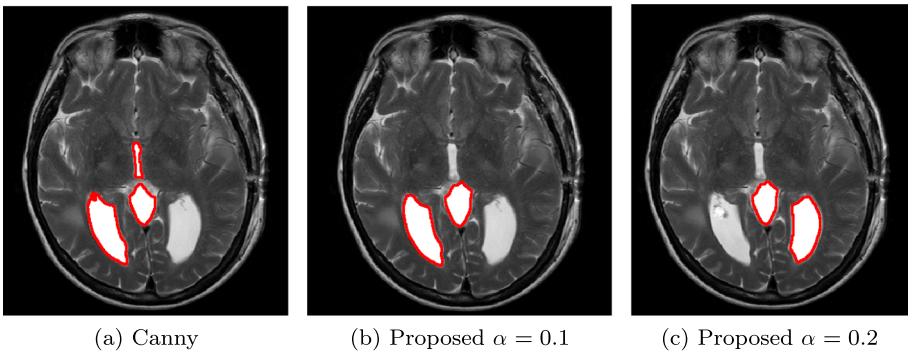

(a) Canny (b) Proposed $\alpha = 0.1$ (c) Proposed $\alpha = 0.2$

(d) Proposed $\alpha = 0.3$ (e) Proposed $\alpha = 0.4$

Figure 8 Segmentation using Medical image-2.

only two regions to the left, $\alpha = 0.3, 0.4,$ and 0.5 also extracted just two regions to the right, $\alpha = 0.6, 0.7,$ and 0.8 increased the number of regions extracted to three. Eventually, the implementation of $\alpha = 0.9$ extracted all the four required regions of interest which fulfilled the expected task.

Segmentation on Medical image-3

In the last Medical image (see Figure 9), the intended purpose was to test if the algorithm can scale efficiently to locate both exterior and interior boundaries. As could be seen in the output image of canny, it was able to extract all the required exterior but not the interior boundaries. The same was observed with the proposed method using $\alpha = 0.1$. In the second attempt with $\alpha = 0.2$, all the interior as well as the exterior boundaries were captured. A perfect segmentation was also achieved for $\alpha = 0.3$ to 0.9 as did $\alpha = 0.2$.

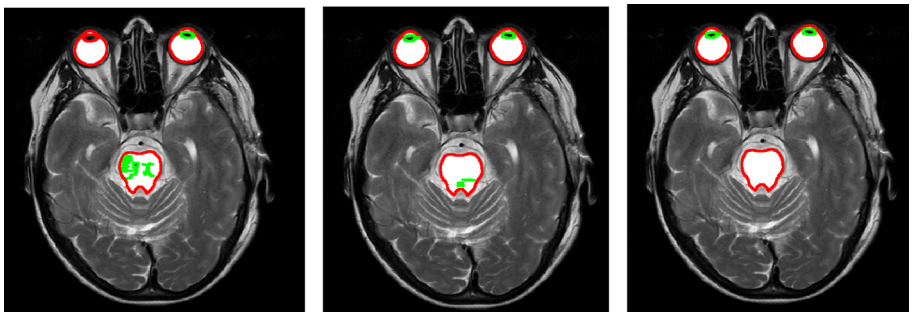

(a) Canny (b) Proposed $\alpha = 0.1$ (c) Proposed $\alpha = 0.2$

Figure 9 Segmentation using Medical image-3.

6 Conclusion

We have presented another way of constructing a fractional-based convolution mask for image edge analysis using the Riemann-Liouville fractional derivative formulation. Unlike other constructions, we extracted the mask, maintaining enough memory without the need for complicated optimization criteria. We performed both quantitative and qualitative comparative analysis with existing edge detectors and have demonstrated the effectiveness and efficiency of the proposed construction in detecting several edge types including step, Dirac edges and hidden edges found in the images used to perform the experiments. In addition, we have shown that the resulting mask is robust to noise. We also performed object identification using the resulting mask and generated mostly significant improvement over the methods studied.

Competing interests
The authors declare that they have no competing interests.

Authors' contributions
All authors contributed equally to the writing of this paper. All authors read and approved the final manuscript.

Acknowledgements
We would like to acknowledge the support received from the National Institute for Mathematical Sciences, Ghana for this study

Received: 8 February 2016 Accepted: 16 August 2016 Published online: 15 September 2016

References

1. Ghimpeteanu, G, Batard, T, Bertalmio, M, Levine, S: A decomposition framework for image denoising algorithms. IEEE Trans. Image Process. **25**, 388-399 (2016)
2. Yan, R, Shao, L: Blind image blur estimation via deep learning. IEEE Trans. Image Process. **25**, 1910-1921 (2016)
3. Jalab, HA, Ibrahim, RW: Texture enhancement based on the Savitzky-Golay fractional differential operator. Math. Probl. Eng. **2013**, Article ID 149289 (2013)
4. Oram, JJ, McWilliams, JC, Stolzenbach, KD: Gradient-based edge detection and feature classification of sea-surface images of the Southern California Bight. Remote Sens. Environ. **112**(5), 2397-2415 (2008)
5. Shrivakshan, GT, Chandrasekar, C: A comparison of various edge detection techniques used in image processing. Int. J. Comput. Sci. Issues **9**(1), 269-276 (2012)
6. Yasri, I, Hamid, NH, Yap, VV: An FPGA implementation of gradient based edge detection algorithm design. In: International Conference on Computer Technology and Development. IEEE Press, New York (2009)
7. El-Sayed, MA: A new algorithm based entropic threshold for edge detection in images. Int. J. Comput. Sci. Issues **8**(1), 71-78 (2011)
8. Guo, W, Lai, M-J: Box spline wavelet frames for image edge analysis. SIAM J. Imaging Sci. **6**(3), 1553-1578 (2013)
9. Yang, Z, Lang, F, Yu, X, Zhang, Y: The construction of fractional differential gradient operator. J. Comput. Inf. Syst. **7**, 4328-4342 (2011)
10. Oustaloup, A, Mathieu, B, Melchior, P: Edge detection using non integer derivation. In: IEEE European Conference on Circuit Theory and Design (ECCTD '91), Copenhagen, Denmark, 3-6 September (1991)
11. Garg, V, Singh, K: An improved Grunwald-Letnikov fractional differential mask for image texture enhancement. Int. J. Adv. Comput. Sci. Appl. **3**(3), 130-135 (2012)

12. Gao, C, Zhou, J, Zhang, W: Edge detection based on the Newton interpolation's fractional differentiation. Int. Arab J. Inf. Technol. **11**(3), 223-228 (2014)
13. Pu, Y, Wang, W, Zhou, J, Wang, Y, Jia, H: Fractional differential approach to detecting textural features of digital image and its fractional differential filter implementation. Sci. China, Ser. F **51**(9), 1319-1339 (2008)
14. Jalab, HA, Ibrahim, RW: Texture feature extraction based on fractional mask convolution with Cesaro means for content-based image retrieval. In: 12th Pacific Rim International Conference on Trends in Artificial Intelligence (PRICAI '12), pp. 170-179 (2012)
15. Dalir, M, Bashour, M: Applications of fractional calculus. Appl. Math. Sci. **4**(21), 1021-1032 (2010)
16. Jalab, HA, Ibrahim, RW: Denoising algorithm based on generalized fractional integral operator with two parameters. Discrete Dyn. Nat. Soc. **2012**, Article ID 529849 (2012)
17. McAndrew, A: An introduction to digital image processing with Matlab notes for SCM2511 image processing. School of Computer Science and Mathematics, Victoria University of Technology (2004)
18. El-Zaart, A: A novel method for edge detection using 2 dimensional gamma distribution. J. Comput. Sci. **6**(2), 199-204 (2010)
19. Roushdy, M: Comparative study of edge detection algorithms applying on the grayscale noisy image using morphological filter. GVIP, special issue on edge detection, 51-59 (2007)
20. Wang, M, Yuan, S: A hybrid genetic algorithm based edge detection method for SAR image. In: IEEE Proceedings of the Radar Conference, 9-12 May, pp. 503-506 (2005)
21. Chan, TF, Vese, LA: Active contours without edges. IEEE Trans. Image Process. **10**, 266-277 (2001)
22. Mumford, D, Shah, J: Optimal approximation by piecewise smooth functions and associated variational problems. Commun. Pure Appl. Math. **42**, 557-685 (1989)
23. He, W, Lai, MJ: Construction of bivariate compactly supported biorthogonal box spline wavelets with arbitrarily high regularities. Appl. Comput. Harmon. Anal. **6**, 53-74 (1999)
24. Lai, MJ: Construction of multivariate compactly supported prewavelets in L_2 spaces and pre-Riesz basis in Sobolev spaces. J. Approx. Theory **142**, 83-115 (2006)
25. Aurich, V, Weule, J: Nonlinear Gaussian filters performing edge preserving diffusion. In: Proceedings of the 17th Deutsche Arbeitsgemeinschaft für Mustererkennung (DAGM) Symposium, Bielefeld, Germany, 13-15 September, pp. 538-545. Springer, Berlin (1995)
26. Basu, M: A Gaussian derivative model for edge enhancement. Pattern Recognit. **27**, 1451-1461 (1994)
27. Deng, G, Cahill, LW: An adaptive Gaussian filter for noise reduction and edge detection. In: Proceedings of the IEEE Nuclear Science Symposium and Medical Imaging Conference, 31 October-6 November, pp. 1615-1619. IEEE Xplore Press, San Francisco (1993)
28. Kang, C, Wang, W: A novel edge detection method based on the maximizing objective function. Pattern Recognit. **40**, 609-618 (2007)
29. Siuzdak, J: A single filter for edge detection. Pattern Recognit. **31**, 1681-1686 (1998)
30. Zhu, Q: Efficient evaluations of edge connectivity and width uniformity. Image Vis. Comput. **14**, 21-34 (1996)
31. Ambrosio, L, Tortorelli, VM: On the approximation of free discontinuity problems. Boll. Unione Mat. Ital., B **7**(6), 105-123 (1992)
32. Osher, S, Sethian, JA: Fronts propagating with curvature-dependent speed: algorithms based on Hamilton-Jacobi formulations. J. Comput. Phys. **79**, 12-49 (1988)
33. Lai, MJ, Stockler, J: Construction of multivariate compactly supported tight wavelet frames. Appl. Comput. Harmon. Anal. **21**, 324-348 (2006)
34. Qi, D, Guo, F, Yu, L: Medical image edge detection based on omnidirectional multi-scale structure element of mathematical morphology. In: Proceedings of the IEEE International Conference on Automation and Logistics, pp. 2281-2286. IEEE, Washington (2007)
35. Stefan, W, Renaut, RA, Gelb, A: Improved total variation-type regularization using higher-order edge detectors. SIAM J. Imaging Sci. **3**, 232-251 (2010)
36. Mahmoodi, S: Edge detection filter based on Mumford-Shah Green function. SIAM J. Imaging Sci. **5**, 343-365 (2012)
37. Zhang, L, Butler, A, Sun, C: Fractal dimension assessment of brain white matter structural complexity post stroke in relation to upper-extremity motor function. Brain Res. **1228**, 229-240 (2008)
38. Hristov, J: Transient heat diffusion with a non-singular fading memory Therm. Sci. **20**(2), 757-762 (2016)
39. Caputo, M, Fabrizio, M: A new definition of fractional derivative without singular kernel. Prog. Fract. Differ. Appl. **2**, 73-85 (2015)
40. Atangana, A, Baleanu, D: New fractional derivatives with non-local and non-singular kernel: theory and application to heat transfer model. Therm. Sci. **20**(2), 763-769 (2016)
41. Ibrahim, RW: On generalized Srivastava-Owa fractional operators in the unit disk. Adv. Differ. Equ. **2011**, 55 (2011)
42. Zhang, Y, Pu, Y, Zhou, J: Construction of fractional differential masks based on Riemann-Liouville definition. J. Comput. Inf. Syst. **6**(10), 3191-3199 (2010)
43. Chen, X, Fei, X: Improving edge-detection algorithm based on fractional differential approach. In: International Conference on Image, Vision and Computing, pp. 1-6 (2012)
44. Loverro, A: Fractional calculus: history, definitions and applications for the engineer. In: Rapport technique, Univeristy of Notre Dame: Department of Aerospace and Mechanical Engineering, pp. 1-28 (2004)
45. Sheikh, HR, Wang, Z, Bovik, AC: LIVE Image Quality Assessment Database, Release 2. http://live.ece.utexas.edu/research/quality (2005). Accessed 25 Jan 2015
46. Ma, X, Li, B, Zhang, Y, Yan, M: The Canny edge detection and its improvement. In: Artificial Intelligence and Computational Intelligence. Lecture Notes in Computer Science, vol. 7530, pp. 50-58 (2012)
47. Wang, Z, Bovik, AC, Sheikh, HR, Simoncelli, EP: Image quality assessment: from error visibility to structural similarity. IEEE Trans. Image Process. **13**(4), 600-612 (2004)